

Supporting Information for

“Sharpened VO₂ phase transition via controlled release of epitaxial strain”

Daesu Lee^{†,‡}, Jaeseong Lee^{§,‡}, Kyung Song^{⊥, #}, Fei Xue[¶], Si-Young Choi^{⊥, #}, Yanjun Ma[†], Jacob Podkaminer[†], Dong Liu[§], Shih-Chia Liu^{||}, Bongwook Chung[▽], Wenjuan Fan[§], Sang June Cho[§], Weidong Zhou^{||}, Jaichan Lee[▽], Long-Qing Chen[¶], Sang Ho Oh^{⊥, •}, Zhenqiang Ma^{, §}, and Chang-Beom Eom^{*, †}*

[†]Department of Materials Science and Engineering, University of Wisconsin-Madison, Madison, Wisconsin 53706, USA.

[§]Department of Electrical and Computer Engineering, University of Wisconsin-Madison, Madison, Wisconsin 53706, USA.

[⊥]Department of Materials Science and Engineering, Pohang University of Science and Technology, Pohang 37673, Korea.

[¶]Department of Materials Science and Engineering, The Pennsylvania State University, University Park, Pennsylvania 16802 USA.

[#]Department of Materials Modeling and Characterization, Korea Institute of Materials Science, Changwon 51508, Korea.

^{||}Department of Electrical Engineering, University of Texas-Arlington, Arlington, Texas 76019, USA.

[▽]School of Advanced Materials Science and Engineering, Sungkyunkwan University, Suwon 16419, Korea.

[•]Department of Energy Science, Sungkyunkwan University, Suwon 16419, Korea.

*E-mail: eom@engr.wisc.edu, mazq@engr.wisc.edu

Thin Film Growth

Epitaxial VO₂ thin films were grown on (001) TiO₂ substrate using the pulsed laser deposition method. Before deposition, low miscut (<0.1°) TiO₂ substrates were cleaned by sonicating with acetone and then rinsing with isopropanol. A SnO₂ epitaxial layer with a thickness of 100 nm was deposited as a bottom template on the TiO₂ substrate. A KrF excimer laser ($\lambda = 248$ nm) beam was focused on SnO₂ and V₂O₅ ceramic targets to an energy density of ~ 2.0 J cm⁻² and pulsed at 5 Hz (for SnO₂ layer) or 10 Hz (for VO₂ layer). SnO₂ layer was grown at a substrate temperature of 400 °C and oxygen partial pressure of 50 mTorr. After growth of SnO₂ layer, VO₂ layer was grown at the temperature of 400°C and oxygen partial pressure of 18 mTorr. After growth, the VO₂ films were cooled down to room temperature at oxygen partial pressure of 18 mTorr.

XRD measurements

We examined structural quality of the films by using high-resolution four-circle X-ray diffraction (XRD) machine (Bruker D8 advance). Figure S1 shows the out-of-plane XRD θ - 2θ scan of 300-nm-thick VO₂ films on (001) TiO₂ and SnO₂/TiO₂ substrates. The XRD pattern shows a clear film peak at $2\theta = 64.8^\circ$ along with the (002) diffraction peaks from underlying rutile SnO₂ and TiO₂ substrate. The film diffraction peak comes from the ($\bar{4}02$) diffraction of monoclinic VO₂, corresponding to the (002) diffraction of high-temperature rutile VO₂ phase. No other peaks are observed by XRD analysis, pointing out that the VO₂ film is highly oriented and with a pure phase. Importantly, the peak position is almost identical to that (i.e., $2\theta \sim 64.7^\circ$) of the ($\bar{4}02$) diffraction for bulk monoclinic VO₂, suggesting that the film is fully relaxed with bulk-like lattices. Also, Fig. S1(d) shows that the film diffraction peak has a symmetric shape [in contrast

to the asymmetric peak shape of the VO₂/TiO₂ film; Fig. S1(c)], implying that the misfit strain is abruptly relaxed without gradual strain relaxation, consistent with our prediction. To obtain further information on lattice strains, we used the X-ray reciprocal space mappings (RSMs), as shown in Figs. 2(c) and (d).

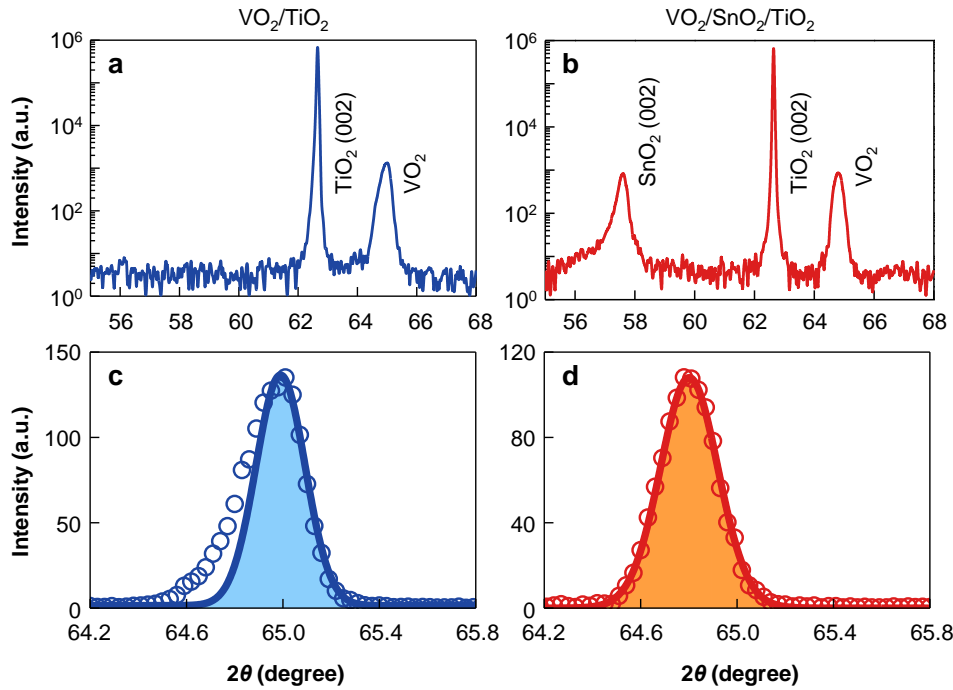


Figure S1. Structural analyses. (a, b) Out-of plane θ - 2θ XRD patterns of 300-nm-thick VO₂ films on (a) TiO₂ and (b) SnO₂/TiO₂. (c, d) Enlarged plots of the film diffraction peak of VO₂ films on (c) TiO₂ and (d) SnO₂/TiO₂. Circles are experimental data, and solid lines indicate the fits by a single-peak Gaussian.

TEM sample preparation and *in situ* heating TEM

Cross-sectional TEM samples for this study were prepared by a conventional way including mechanical grinding to a thickness of 80 μm and dimpling to a thickness of less than 10 μm . The

mechanically polished samples were ion-milled using 3 kV Ar⁺ ion beam (PIPS, Gatan, USA) and then using a low energy (0.7 kV) Ar⁺ ion beam to remove a surface damage layer. *In situ* heating experiments were performed in a field-emission TEM (JEM-2100F, JEOL, Japan) operated at 200 kV. For *in situ* heating observation, the samples were heated up to 363 K with a heating rate of 5 K min⁻¹ using a double tilt heating holder (Model 652-Ta, Gatan, USA) and then allowed to cool down to room temperature. Real time movies during the heating-cooling cycle were acquired in dark-field TEM mode to distinguish the monoclinic/rutile phase domains, with CCD camera (ORIOUS 200D, Gatan) at 25 frames s⁻¹ (Supporting Movies 3 –5).

Inline electron holography.

Two-dimensional (2-D) strain maps were obtained by dark-field inline electron holography [Figs. 2(g) and (h) and Fig. S2]. Through-focal series of dark-field TEM images, the input data for dark-field inline electron holography, were obtained using a JEOL 2100F, equipped with a 200 kV field emission gun. The Gatan's GIF Tridiem imaging filter was used to remove inelastically scattered electrons around the selected diffracted beam. The width of energy window was ± 7.5 eV. An objective aperture of 10 μm in diameter was placed on the microscope's optical axis to select a specific diffracted beam. The size of this aperture limited the spatial resolution to 0.8 nm. For the out-of-plane strain mapping, the incident electron beam was tilted in such a way that the excited (002)_s reflection was aligned parallel to the optical axis of the microscope, where the subscript *s* denotes the substrate (i.e., TiO₂). The (200) reflection was chosen for mapping the in-plane strain. Through-focal dark-field TEM images were recorded by changing the defocus value from -8 μm to +8 μm using a 2048×2048 pixels fiber-optically coupled UltraScan 1000 FT (Gatan, Inc.) camera. The 2-D electron phase information was reconstructed from TEM images

using the full resolution wave reconstruction (FRWR) software.^{S1,S2}. Figure S2 shows 2-D out-of-plane lattice strain maps and profiles of 300-nm-thick VO₂ films on (001) TiO₂ and SnO₂/TiO₂ substrates. The map clearly visualizes the distribution of different c-axis lattice parameters at a spatial resolution of ~0.8 nm and a strain resolution of ±0.1%.

In VO₂ films on TiO₂ [Fig. S3(a)], the out-of-plane strain was around -1.8 % near the bottom interface due to the misfit strain, and it became relaxed and negligible near the top surface or cracks. On the other hand, the VO₂ film on SnO₂/TiO₂ shows no recognizable strain feature within VO₂ film, demonstrating that the VO₂/SnO₂/TiO₂ film exhibited uniform bulk-like lattice without any crack and noticeable inhomogeneity.

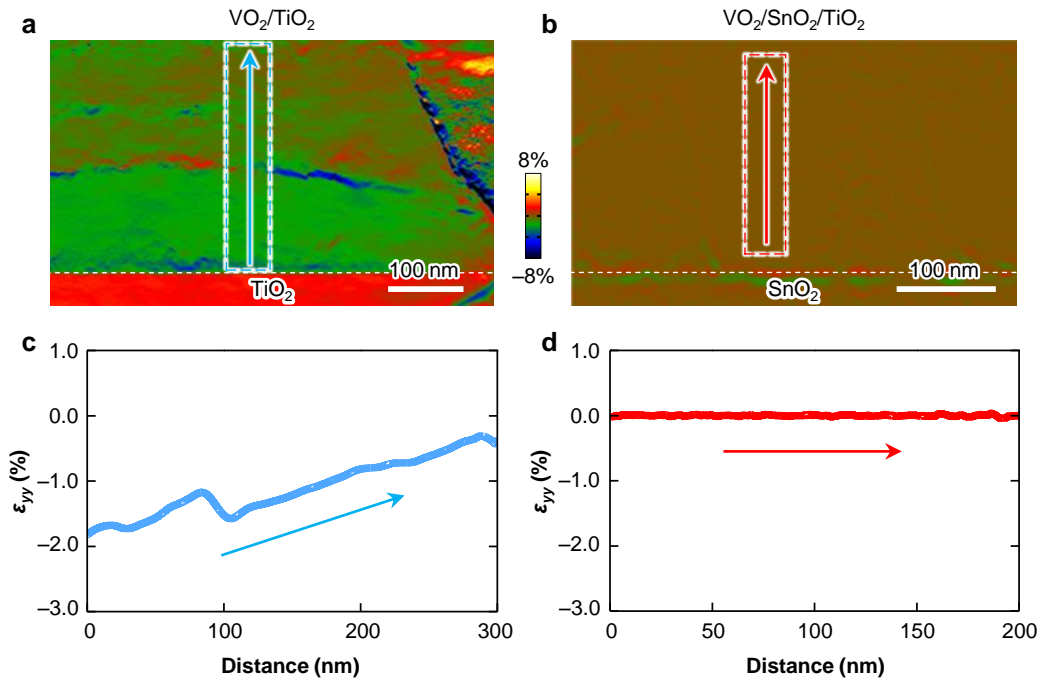


Figure S2. Local strain maps in epitaxial VO₂ films. (a, b) Spatial map of the out-of-plane strain ϵ_{yy} [i.e., $(c_{\text{film}} - c_{\text{bulk}})/c_{\text{bulk}}$] of VO₂ films on (a) TiO₂ and (b) SnO₂/TiO₂. (c, d) Profile of ϵ_{yy} in selected areas of VO₂ films on (c) TiO₂ and (d) SnO₂/TiO₂.

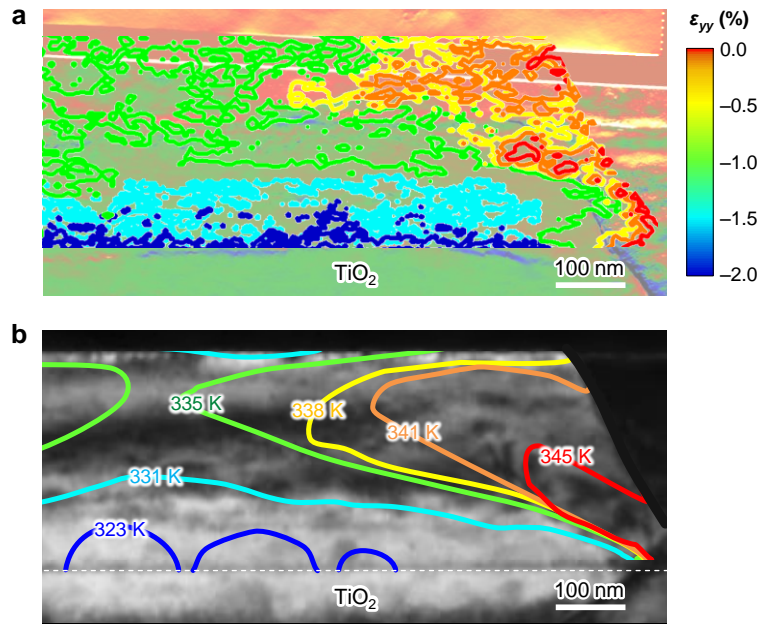


Figure S3. Comparison between local strain and local phase evolution. (a) Some equi-strain lines are overlapped onto the measured strain map [Fig. 2(g)]. (b) Experimentally measured location of phase boundaries between monoclinic and rutile structures on heating. Phase boundaries at each temperature are from *in situ* TEM data in Fig. 3(a). The background image is the dark field TEM image at 345 K. Phase boundaries are presented by solid lines with different colors, ranging from blue (low temperature) to red (high temperature).

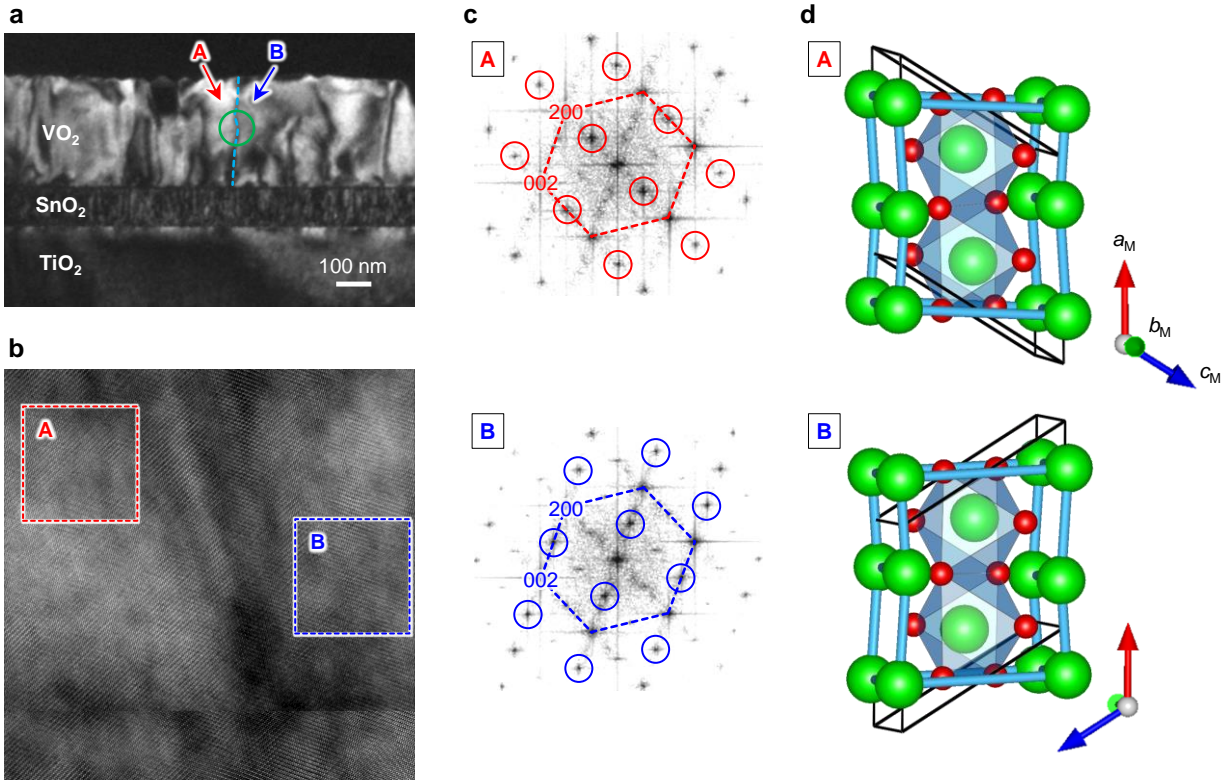


Figure S4. Domain boundary in VO₂ film on SnO₂/TiO₂. (a) TEM image of VO₂ film on SnO₂/TiO₂. Blue dashed line represents the boundary between two monoclinic domains A and B. Note that VO₂ films on TiO₂ or SnO₂/TiO₂ substrates can intrinsically have four different domain variants in the monoclinic phase, which are rotated by 90° along the a_M axis from each other (see also Fig. S8). (b) High-resolution TEM image for the region, denoted by green circle in (a). (c) Crystallographic orientation of the boxed regions in (b) (i.e., A and B regions) is determined by using nano-beam electron diffractions. Superstructure spots (denoted by circles) originate from the monoclinic distortion. Along with these strong superstructure peaks, other weak superstructure peaks were also observed, which could originate from some overlapped domains in a thick TEM specimen. (Note that for *in situ* TEM experiments, we used a relatively thick TEM specimen.) (d) Monoclinic orientations for A and B domains, determined based on the electron diffraction patterns in (c).

STEM-EELS analysis

Identical TEM samples were used for STEM-EELS analysis. Atomic structural analysis and EELS (Electron Energy Loss Spectroscopy) analysis were performed in a scanning transmission electron microscope (JEM-2100F, JEOL, Japan) at 200 kV with a probe corrector (CEOS GmbH, Germany) and GIF Quantum with dual EELS (Quantum 965, Gatan, USA). The collection semi-angles of the HAADF (High Angle Annular Dark Field) and LAADF (Low Angle Annular Dark Field) detectors were from 90 to 220 mrad and from 30 to 60 mrad, respectively. The optimum size of the electron probe was 0.9 Å and energy resolution of EELS was confirmed to be 0.8 eV by the full width at half maximum (FWHM) of the zero loss peak. The LAADF-STEM images provide the information of the strained regions from the collection of low-order diffractions of electrons via LAADF detector close to the on-axis.^{S3,S4} The LAADF-STEM images in Figs. 2(a) and (b) show the distinctive strain distribution in VO₂ film by adopting SnO₂ layer; whilst strain is accumulated along the interface [Fig. 2(a)], the residual strain is largely disappeared by the SnO₂ layer [Fig. 2(b)]. Such a strain-free VO₂ film can give rise to no undesirable, extrinsic effects such as the oxygen vacancies and valence state variation. To clarify the chemical and structural homogeneity, we obtained O-*K* edge and V-*L* edge spectrums from the VO₂ film on SnO₂/TiO₂ as shown in Fig. S5. Valance state change in vanadium, from +4 to +3, largely shifts the onset position of V-*L* edge by 1.2 ~ 2 eV and increase *L*₃ to *L*₂ ratio by 10%.^{S5,S6} Similar V-*L* edges near the interface and off the interface [Fig. S5(b)] make sure of the chemical homogeneity, indicative of no oxygen vacancies as well as +4 of vanadium valance state. By taking closer look at the interface in Fig. S5(c), we found that the chemical homogeneity is maintained close to the interface between VO₂ and SnO₂ since O-*K* edge in SnO₂ (indicated by the green arrow) is clearly differentiated by O-*K* edge in VO₂ (indicated by the orange arrow).

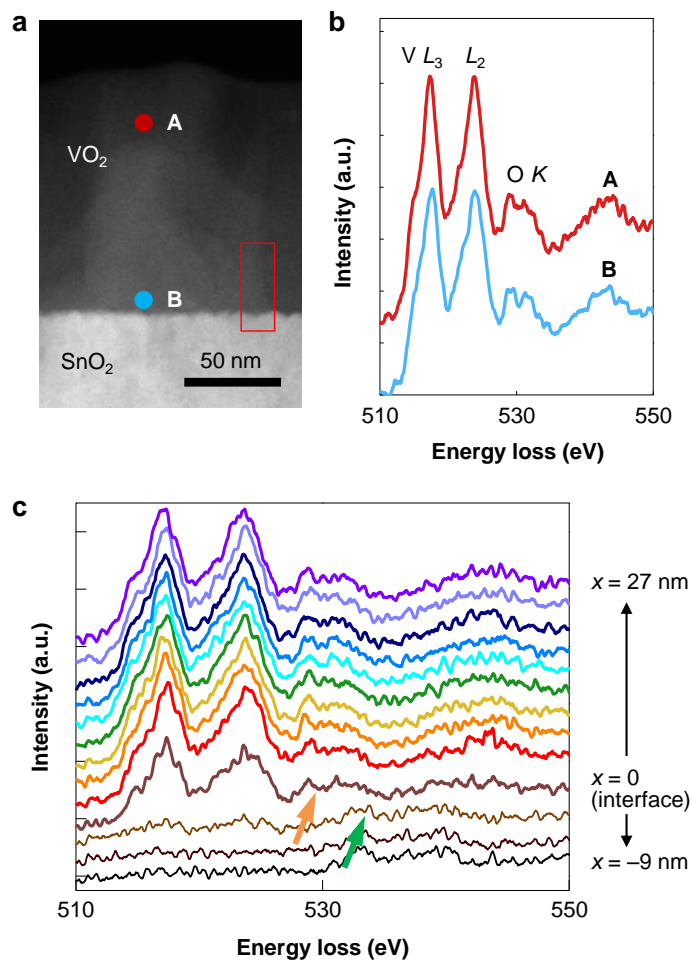


Figure S5. Chemical homogeneity in VO₂ film on SnO₂/TiO₂. (a, b) (a) Local TEM image and (b) the corresponding local electron energy loss (EELS) spectra in VO₂ film on SnO₂/TiO₂. (c) A series of EELS spectra [red-lined box in (a)], measured from the underlying SnO₂ layer to the VO₂ film with a spatial interval of ~3 nm. On moving from the interface to the VO₂ film, the V $L_{2,3}$ edges, in terms of L_3/L_2 intensity ratio and position, remain essentially unchanged, which indicates that our VO₂ film is not only chemically homogeneous (i.e., maintaining the V oxidation state of 4+), but also structurally homogeneous (i.e., maintaining the same V–O bond length).

Crack formation

We explored the contribution of SnO₂ template to protect the VO₂ films against the cracking. VO₂ bulk crystals and epitaxial films tend to crack during phase transition and degrade upon repeated cycling. During SPT on cooling, rutile phase becomes monoclinically distorted with the formation of monoclinic domains. The domain formation simultaneously causes strong internal stress near domain boundaries, whose value may locally exceed a critical strength and causes cracking [Fig. S6(a)], especially in the case of large-sized single crystals. We therefore expect that such crack formation could be avoided in epitaxial VO₂ films that consist of small domains in their as-grown state [Fig. S6(b)].

We found that cracks were increasingly formed upon repeated thermal cycles and severely affected the MIT features in VO₂ films on bare TiO₂ [Figs. S6(c) and S7]. The increase of resistance by cracks was more significant for the nominally metallic phase, and as a result, the magnitude of resistance change across the MIT was much reduced down to $\sim 10^5$ % [Fig. S7(b)]. On the other hand, the VO₂ films on SnO₂/TiO₂ shows quite robust MIT, whose magnitude of resistance change remained well conserved as $\sim 10^6$ % even after 1,000 cycles [Fig. S7(d)].

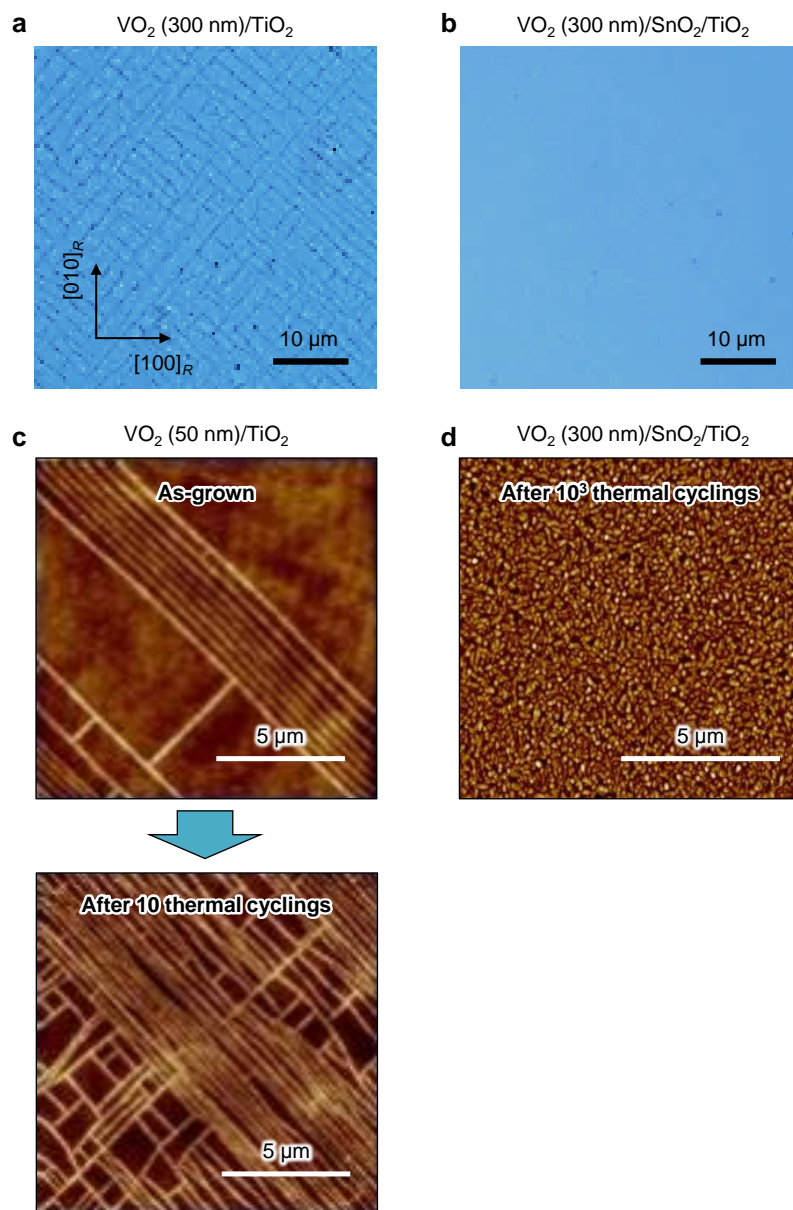


Figure S6. Cracks in epitaxial VO₂ films. (a, b) Optical microscope images for 300-nm-thick VO₂ films on (a) TiO₂ and (b) SnO₂/TiO₂. (a) clearly shows the rectangular network of cracks. (c, d) Surface images of (c) 50-nm-thick VO₂ film on TiO₂ and (d) 300-nm-thick VO₂ film on SnO₂/TiO₂, measured by atomic force microscope. (c) exhibits the additional formation of cracks by repeated thermal cycles. Surface images of VO₂ film on SnO₂/TiO₂ didn't show any change after thermal cyclings.

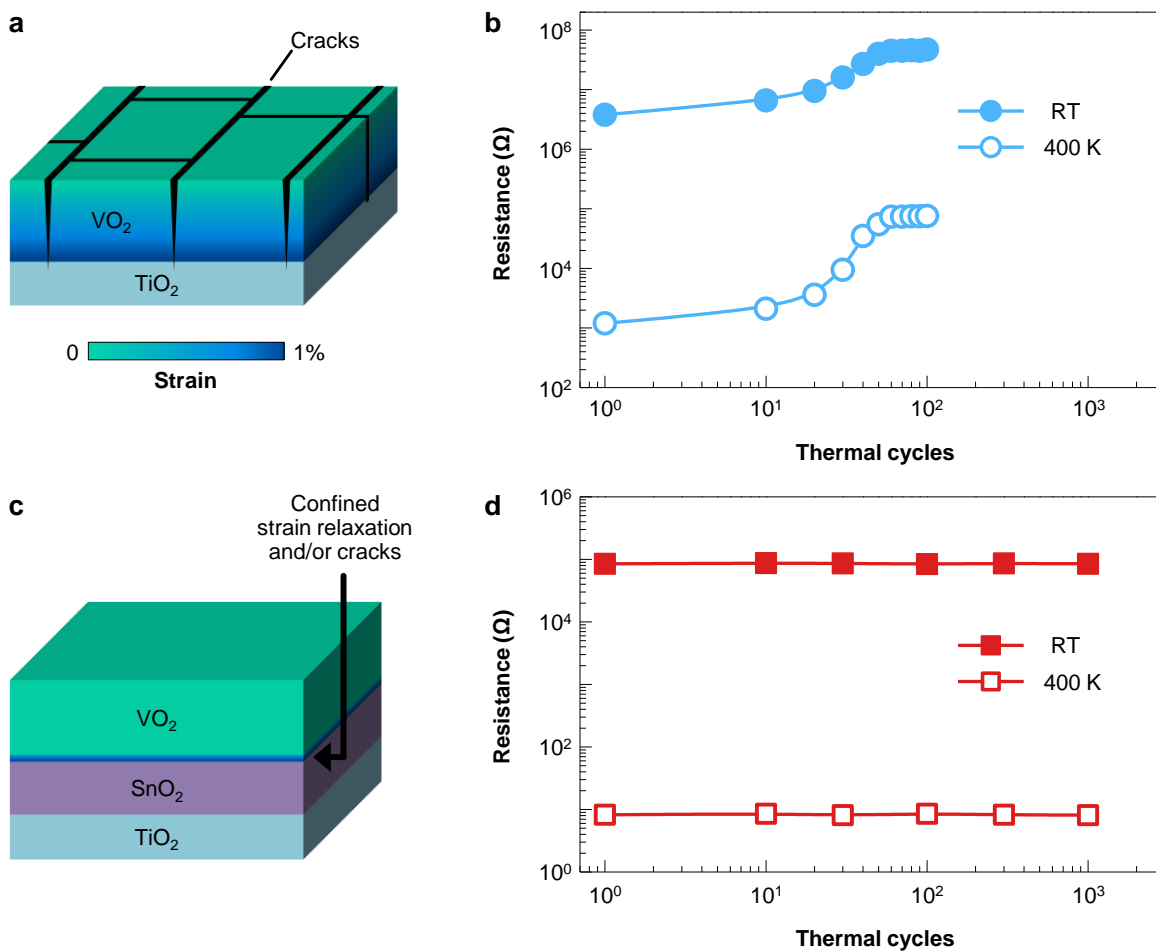


Figure S7. Stability against the cracking. (a, c) Schematic drawings showing the strain relaxation and cracking in VO₂ films (a) without and (c) with SnO₂ template. In the VO₂ films on SnO₂-templated TiO₂, severe structural defects, such as strain relaxation and cracks, are expected to be well confined near the interface, which protects the films against degradation by repeated thermal cycles. (b, d) Resistance, measured at room temperature and 400 K, after repeated phase transitions of VO₂ films (b) without and (d) with SnO₂ template.

Phase diagram calculation

According to the Landau theory, the phase transition in VO₂ can be described by a structural order parameter η , with $\eta=0$ and $\eta \neq 0$ representing the rutile and monoclinic phases, respectively. The total free energy density is given by

$$f = \frac{1}{2}A_2\eta^2 + \frac{1}{4}A_4\eta^4 + \frac{1}{6}A_6\eta^6 + \frac{1}{2}c_{ijkl}(\varepsilon_{ij} - \varepsilon_{ij}^0)(\varepsilon_{kl} - \varepsilon_{kl}^0), \quad (\text{S1})$$

where A_2 , A_4 , and A_6 are coefficients of the Landau polynomial under stress-free boundary conditions, c_{ijkl} is the elastic stiffness tensor, and ε_{ij} and ε_{ij}^0 are the total strain and eigen strain, respectively. The eigen strain is related to the structural order parameter through $\varepsilon_{ij}^0 = \varepsilon_{ij}^{00}\eta^2$, where ε_{ij}^{00} is the stress-free transformation strain from the rutile to monoclinic phase transition.^{S7}

Among all the coefficients, only A_2 is assumed to be dependent on temperature, i.e., $A_2 = A_0[T - T_c]$, where A_0 is a constant and T_c is the Curie temperature. The details about the procedure of obtaining the Landau coefficients can be found in refs. S8 and S9. In the calculation, we use the value $A_0 = 1.42 \times 10^6 \text{ N m}^{-2}$, $T_c = 325 \text{ K}$, $A_4 = -7.12 \times 10^6 \text{ N m}^{-2}$, $A_6 = -5.34 \times 10^7 \text{ N m}^{-2}$, which are fitted based on the values of transformation enthalpy in ref. S8 and transition temperature in this work. Young's modulus $E = 155 \text{ GPa}$, Poisson's ratio $\nu = 0.287$, which take the values from ref. S9. ε_{ij}^{00} takes the value from ref. S8.

The strain-temperature phase diagram is obtained by applying the thin film boundary conditions, i.e.,

$$\varepsilon_{11} = \varepsilon_{22} = \varepsilon_s, \quad \varepsilon_{12} = 0, \quad \frac{\partial f}{\partial \varepsilon_{13}} = 0, \quad \frac{\partial f}{\partial \varepsilon_{23}} = 0, \quad \frac{\partial f}{\partial \varepsilon_{33}} = 0, \quad (\text{S2})$$

where ε_s is the biaxial epitaxial strain. Equation (S2) indicates that ε_s is fixed by the substrate, with the out-of-plane direction stress-free. Through minimizing the free energy density in Eq.

(S1) under the thin-film boundary conditions,^{S8} we can calculate the stable phases at different temperatures and epitaxial strains, which are plotted in Fig. 1(a).

Phase-field simulations

The domain structure is evolved by solving the time-dependent phase-field equations

$$\frac{\delta\eta}{\delta t} = L \frac{\delta F}{\delta\eta}, \quad (\text{S3})$$

where t is time, L is the kinetic coefficient related to the domain wall mobility and F is the total free energy, which is expressed by

$$F = \int [f + \frac{1}{2} g ((\frac{\partial\eta}{\partial x_1})^2 + (\frac{\partial\eta}{\partial x_2})^2 + (\frac{\partial\eta}{\partial x_3})^2)] dV, \quad (\text{S4})$$

where g is the gradient energy coefficient, x_i is the spatial coordinate, and V is the system volume.

In the x_1 and x_2 directions, we assume periodic boundary conditions, whereas a superposition method is used along the x_3 direction.^{S10} For the constrained film, we assume that the top surface is assumed to be stress-free while the bottom interface is coherently clamped by the substrate.^{S10} For the membrane, we assume that both the top surface and bottom interface is stress free. Equation (S3) is solved based on a semi-implicit Fourier-spectral method.^{S11} The system size is $128\Delta x \times 128\Delta x \times 52\Delta x$ and the grid spacing is $\Delta x = 0.42$ nm. Two types of strain conditions are applied to the VO₂ films in the phase-field simulations.

(1) Uniform strain

$$\varepsilon_{11}(x, y, z) = \varepsilon_{22}(x, y, z) = -0.0056, \quad (\text{S5})$$

which corresponds to the red line in Fig. 1(b) and the simulations in (B) of Fig. 1(c);

(2) Strain gradient in both the out-of-plane and in-plane direction

$$\varepsilon_{11}(x, y, z) = \begin{cases} -0.0056, & z \geq \frac{39x+780}{63}, \text{ or } z \geq \frac{-39x+5811}{63} \\ -0.0056 + \frac{0.0146}{2457}(39x-63z+780), & x \leq 64, \text{ and } z < \frac{39x+780}{63} \\ -0.0056 - \frac{0.0146}{2457}(39x+63z-5811), & x > 64, \text{ and } z < \frac{-39x+5811}{63} \end{cases}, \quad (\text{S6})$$

$$\varepsilon_{22}(x, y, z) = \varepsilon_{11}(x, y, z)$$

which describes the strain distribution with two cracks near the top right and top left of the system, and corresponds to the blue line in Fig. 1(b) and the simulations in (A) of Fig. 1(c).

Assume that the interfacial energy between monoclinic and rutile phases is γ_{RM} , and the interfacial energy between two monoclinic domains is γ_{MM} . Due to the distinct crystal structure and lattice parameters (i.e., $a_R = b_R = 4.556 \text{ \AA}$ & $c_R = 2.859 \text{ \AA}$; $a_M = 5.743 \text{ \AA}$, $b_M = 4.517 \text{ \AA}$, $c_M = 5.375 \text{ \AA}$ & $\beta = 122.6^\circ$; see also Fig. S8a), γ_{RM} should be large compared to γ_{MM} . Moreover, γ_{RM} is not only structural interfacial energy, but also metal-insulator interfacial energy,^{S12,S13} whereas γ_{MM} refers to pure ferroelastic domain wall energy with the magnitude $\gamma_{MM} \sim 10 \text{ mJ m}^{-2}$.^{S14,S15} As a result, γ_{RM} can be much larger than γ_{MM} (i.e., interfacial energy ratio $\alpha = \frac{\gamma_{MM}}{\gamma_{RM}} \rightarrow 0$),

making the effect of monoclinic domain boundaries negligible. To describe different monoclinic domains in the phase-field simulations, the phase-transition transformation strain ε_{ij}^{00} is assumed to be position dependent, and the spatial distribution is fixed during the evolution of Equation (S3). Note that ε_{ij}^{00} in different positions is related by the rotation symmetry. The simulation setting is used to reflect the small interfacial energy ratio α . We increase the temperature of the system by 1 K for every 10,000 simulation steps. Since the monoclinic to rutile phase transition is first-order and completed through nucleation and growth, numbers of small nuclei of the rutile phase are artificially added to the system at random positions at the first simulation step after the

temperature is increased. The simulated domain evolution [Fig. 1(c)] well reflected experimental observations [Fig. 3(a)]. Supporting Movies 1 and 2 are also given for the (A) and (B) cases in Fig. 1(c), respectively. We experimentally confirmed that the phase transition dynamics was not much affected by the domain boundary [Fig. 3(b) and Fig. S8].

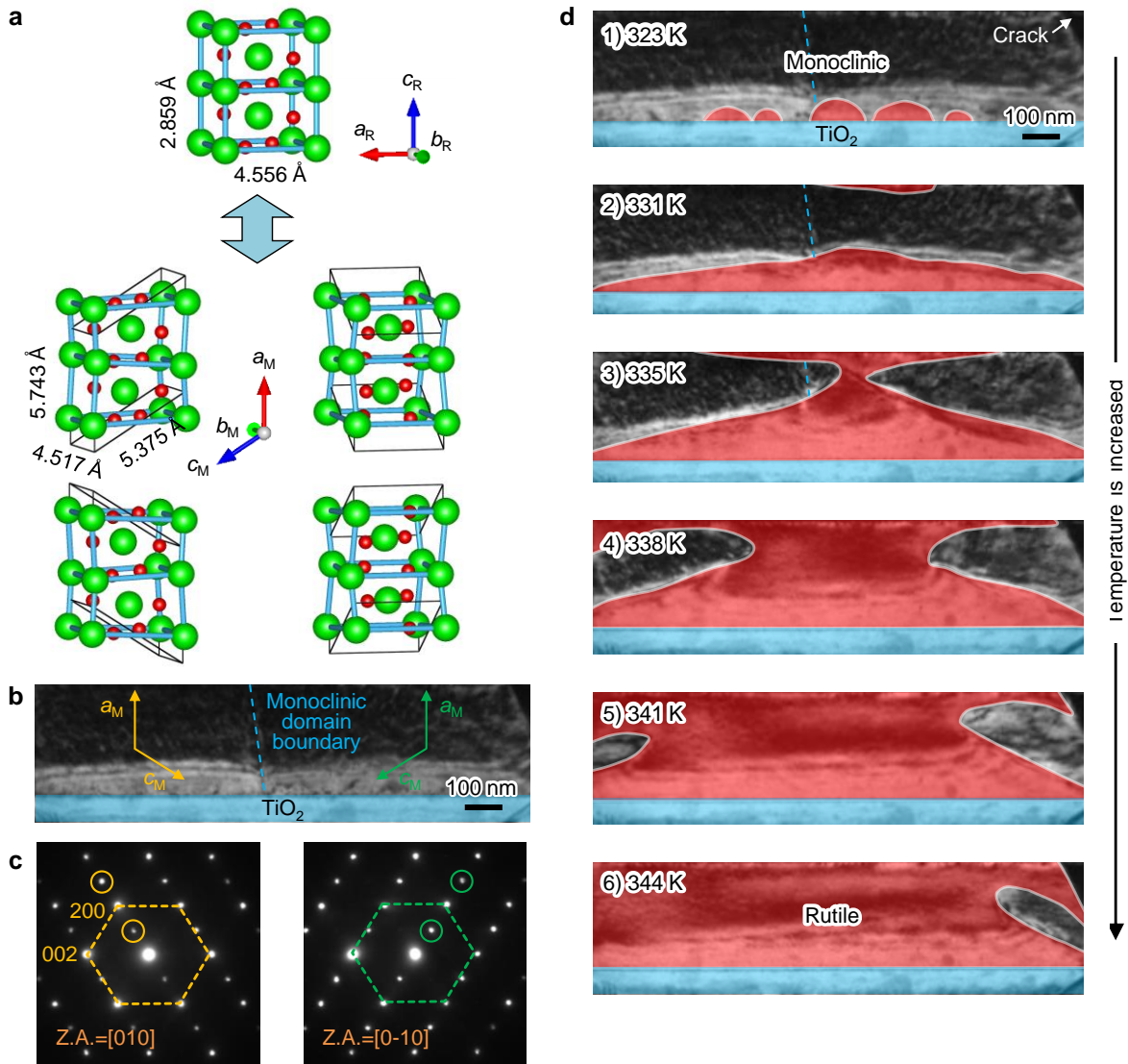


Figure S8. Negligible effect of monoclinic domain boundary during phase transitions. (a) Atomic structures of rutile (upper panel) and monoclinic (lower panel) VO₂. Note that VO₂ films on TiO₂ or SnO₂/TiO₂ substrates can intrinsically have four different domain variants in the

monoclinic phase, which are rotated by 90° along the a_M axis from each other. (b) TEM image of VO_2 film on TiO_2 , showing the monoclinic domain boundary (denoted by blue dashed line). (c) Crystallographic orientation of each monoclinic domain is determined by using nano-beam electron diffractions. Diffracted spots denoted by circles originate from the monoclinic distortion. (d) Monoclinic-to-rutile SPT dynamics on heating, which is not affected by the monoclinic domain boundary (denoted by blue dashed line).

Stress distribution calculation

The stress distribution from the phase-field simulation is plotted in Fig. S9. From Figs. S9(c) and (e), the monoclinic domain walls have large effect on the stress distribution. For single monoclinic domain, the stress is concentrated near the monoclinic-rutile phase boundaries. For the multiple monoclinic domains, however, the stress is concentrated at both the monoclinic-rutile phase boundaries and domain wall-interface intersections.

The mechanical boundary conditions are found to have significant effect on the stress distribution. When both the two interfaces are subject to stress free boundary conditions, the local stress is largely reduced, by comparing Fig. S9(c) with Fig. S9(d) [or by comparing Fig. S9(e) with Fig. S9(f)]. For the coherently grown films, it can be well modelled by boundary conditions of stress-free top surface and constrained bottom interface (constrained bottom interface means that the displacement from the film to the substrate is continuous). For the incoherently grown films, the boundary conditions may be complex, and should be between the two limiting cases of constrained film and membranes. The simulation results in Fig. S9 show that the mechanical boundary conditions of the incoherent interface play an important role in relieving the stress and preventing the formation of cracks during SPT.

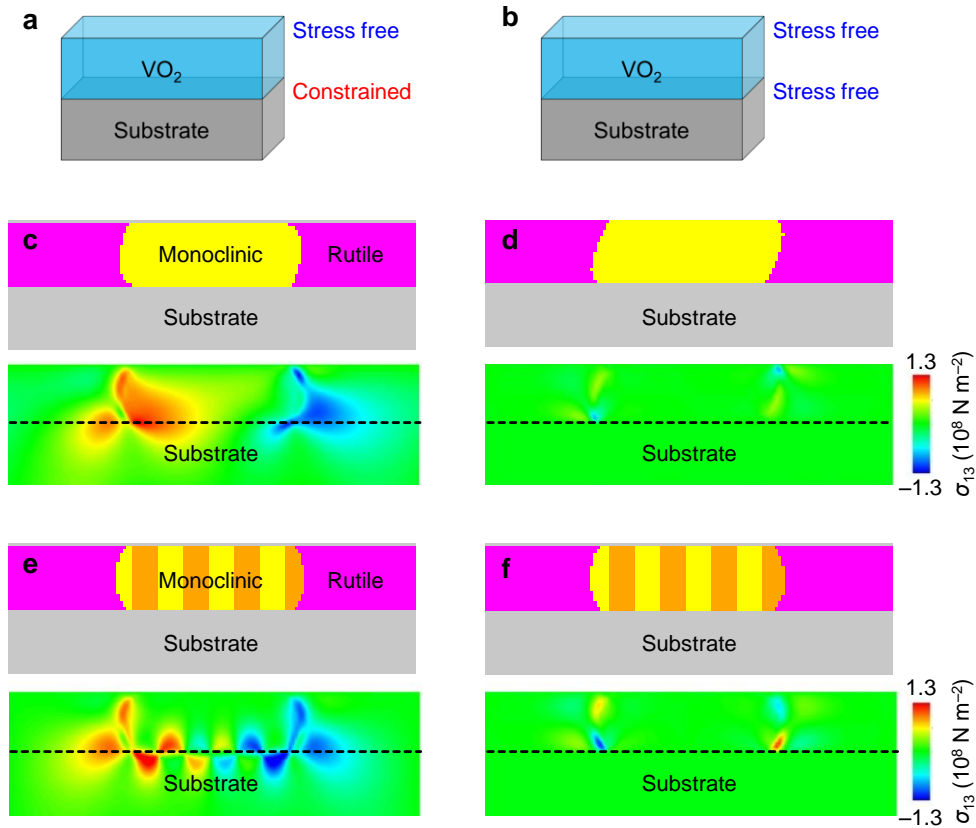


Figure S9. Stress distribution in VO₂ films during SPT. (a, b) Schematics for VO₂ films (a) with lattice-constrained bottom interface and (b) with stress-free bottom interface. (c, d) Calculated stress distribution near the boundaries between monodomain monoclinic and rutile phases for VO₂ films (c) with lattice-constrained bottom interface and (d) with stress-free bottom interface. Upper and lower panels indicate the monoclinic/rutile phase distribution and corresponding stress distribution, respectively. (e, f) Calculated stress distribution near the boundaries between multi-domain monoclinic and rutile phases for VO₂ films (e) with lattice-constrained bottom interface and (f) with stress-free bottom interface. Upper and lower panels indicate the monoclinic/rutile phase distribution and corresponding stress distribution, respectively.

Electrical and Optical Measurements

Using the standard four-contact van der Pauw method with contacts of Al, we measured the electrical resistivity in vacuum as the function of temperature in VO₂ films with or without SnO₂ template [Figs. 3(d) and S10]. As the reference, we also measured the electrical transport for the fully coherent 8-nm-thick VO₂ film on TiO₂ substrate. We quantitatively estimated the sharpness of MIT for the SnO₂-templated film to be ~0.7 K, by using the full-width-at-half-maximum (FWHM) of the derivative curves [Fig. S10(b)]. This sharpness is comparable to that of fully coherent 8-nm-thick VO₂ films on bare TiO₂, which is expected to show the sharpest MIT among VO₂ films.

Using spectroscopic ellipsometry, we measured the refractive index n and extinction coefficient k as a function of temperature (Fig. S11). Figures S11(a) and (b) show the n values, measured during heating, as functions of temperature and the wavelength λ of incident light for 300-nm-thick VO₂ films. For the VO₂ film on bare TiO₂ substrate, the n exhibited gradual change across MIT. On the other hand, for the VO₂ film on SnO₂-templated TiO₂, the n showed abrupt change for every λ across MIT.

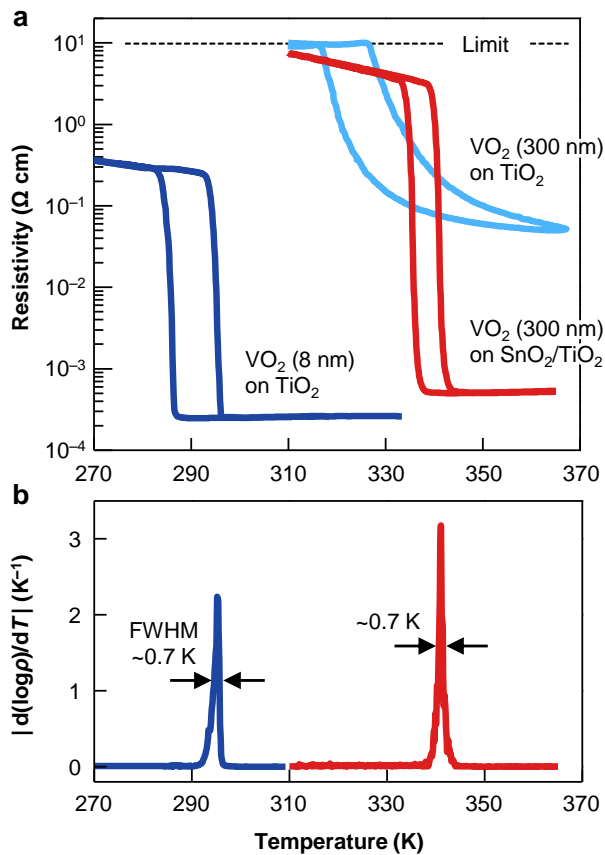


Figure S10. MIT in epitaxial VO₂ films. (a) Resistivity ρ versus temperature for VO₂ films. (b) Derivative curves of ρ for fully coherent 8-nm-thick VO₂ film on TiO₂ (blue solid line) and 300-nm-thick VO₂ film on SnO₂/TiO₂ (red solid line). Data in (b) are obtained on heating.

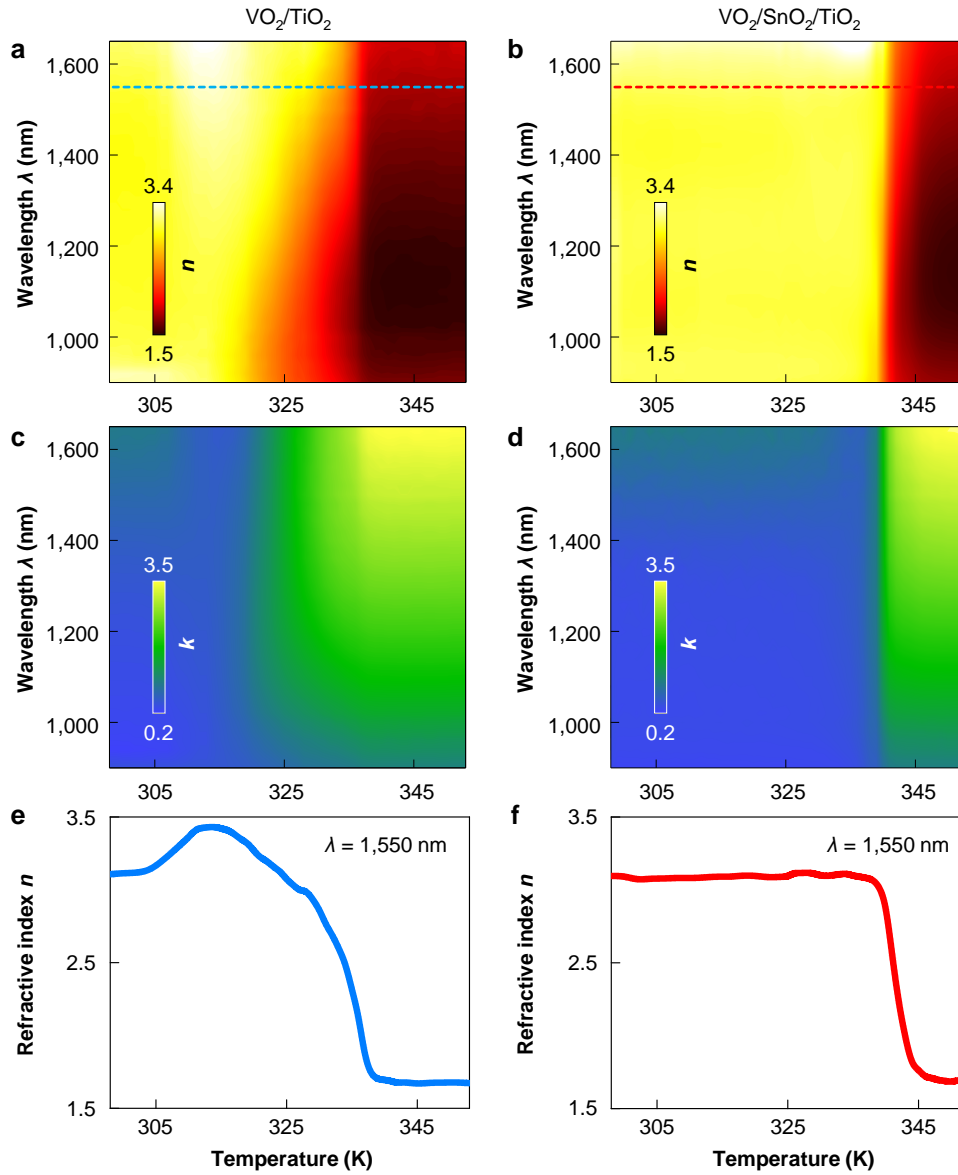


Figure S11. Optical transition in VO₂ films. (a, b) Refractive index n as functions of temperature and wavelength λ for 300-nm-thick VO₂ films on (a) TiO₂ and (b) SnO₂/TiO₂. Dashed lines indicate the case of $\lambda = 1,550$ nm. (c, d) Extinction coefficient k as functions of temperature and wavelength λ for 300-nm-thick VO₂ films on (c) TiO₂ and (d) SnO₂/TiO₂. (e, f) Refractive index n as functions of temperature at a fixed $\lambda = 1,550$ nm for 300-nm-thick VO₂ films on (e) TiO₂ and (f) SnO₂/TiO₂. Data are obtained on heating.

Fabrication and characterization of optical modulators

Si-VO₂ optical modulator was constructed on VO₂ layer with transfer printed Si nanomembrane (NM) [Fig. S12(a)]. First, VO₂ film was patterned by photolithography and reactive ion etching (RIE) in the CF₄ gas. Then, Si nanomembrane was prepared with silicon-on-insulator substrate (SOI, Soitec) with 205-nm-thick Si layer and 400-nm-thick buried oxide (BOX) SiO₂ layer. To make desired Si thickness of 190 nm, top Si layer on SOI was thinned down using thermal oxidation followed by wet etching of oxidation layer in HF. Etching holes are patterned on Si layer by photolithography and reactive ion etching in SF₆/O₂. Si NM transfer onto VO₂ was performed by an elastomeric polydimethylsiloxane (PDMS) stamp transfer printing method [Fig. S12(b)].^{S16,S17} During the transfer, adhesive layer (Su-8 2000.5, Microchem) is spin-coated on VO₂. Since the adhesive layer also serves as an optical cladding layer, thickness was adjusted to ~150 nm to maximize optical switching performance. After the transfer print, Si waveguide is defined by e-beam lithography and inductively coupled plasma etching in Cl₂. Exposed adhesive Su-8 layer is also etched by RIE in O₂. Finally, metal electrodes of 10-nm-thick Ti and 300-nm-thick Au were formed by additional e-beam lithography, e-beam evaporation and lift off. To measure optical switching performance, tunable laser (Tunics Plus) and optical oscilloscope (Agilent 86116A) were used. The laser was coupled into Si waveguide with single mode lensed fibers. Wide wavelength range of the input signal (1.5 μm to 1.6 μm with 0.25-μm step) is used to demonstrate wide bandwidth of the optical switch. The output optical signal from the Si waveguide was also coupled to single mode lensed fiber and sent to oscilloscope. During the measurement, 15-V peak to peak (in the range of 0 V to 15 V) square wave in 1-MHz frequency was applied to Au electrode by function generator (Tektronix FG5010). A 1 kΩ resistor was connected in series to the optical switch to suppress the current level and avoid burning the device.

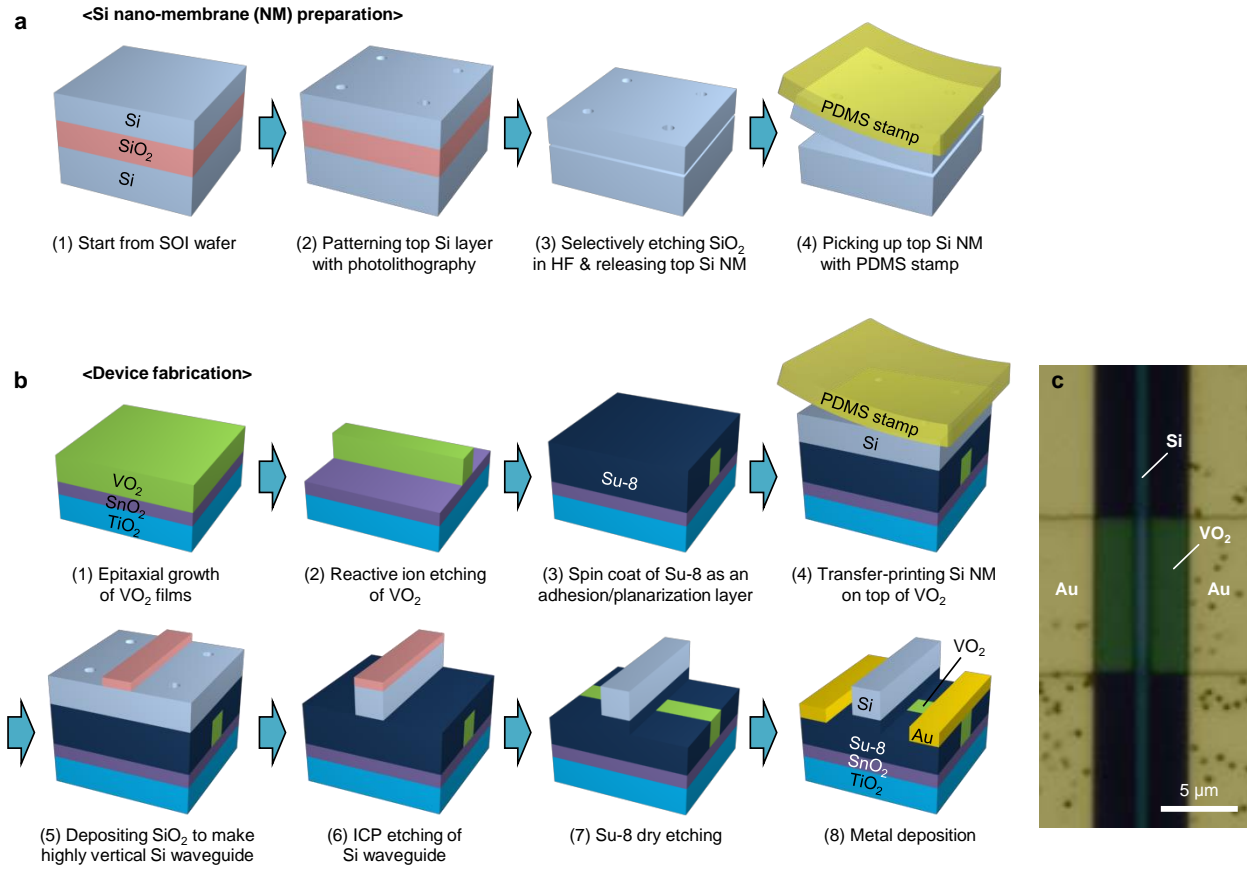


Figure S12. Fabrication of Si-VO₂ optical modulators. (a) Process for preparing Si nano-membrane (NM). (b) Process for fabricating an optical modulator using Si NM and epitaxial VO₂ films. (c) Scanning electron microscope image of the Si-VO₂ optical modulator.

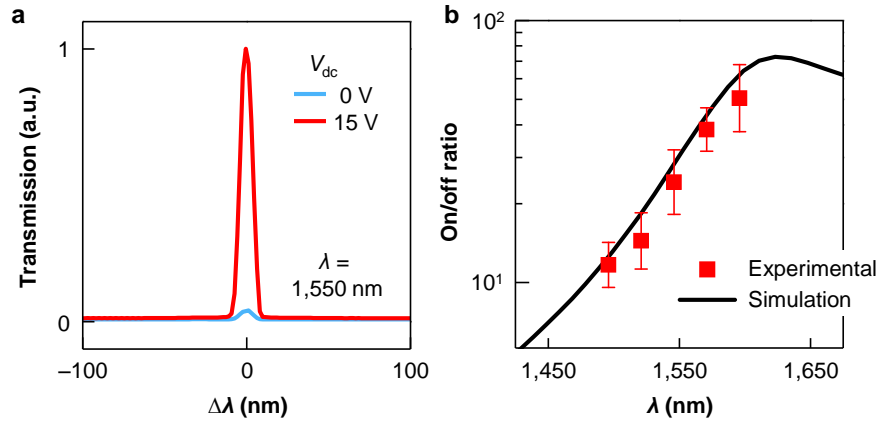


Figure S13. Electrically switchable light transmission in Si-VO₂ optical modulators. (a) Light transmission for the off (i.e., $V_{dc} = 0$ V) and on (i.e., $V_{dc} = 15$ V) state for a fixed wavelength λ of 1,550 nm. (b) The on/off ratio of transmission as a function of λ . Red squares and black solid line correspond to the experimental and simulated results, respectively.

References for Supporting Information

- (S1) Koch, C. T. *Ultramicroscopy* **2008**, *108*, 141–150.
- (S2) Koch, C. T. *Micron* **2014**, *63*, 69–75.
- (S3) Muller, D. A.; Nakagawa, N.; Ohtomo, A.; Grazul, J. L.; Hwang, H. Y. *Nature* **2004**, *430*, 657–661.
- (S4) Choi, S. Y.; Kim, S.-D.; Choi, M.; Lee, H.-S.; Ryu, J.; Shibata, N.; Mizoguchi, T.; Tochigi, E.; Yamamoto, T.; Kang, S.-J. L.; Ikuhara, Y. *Nano Lett.* **2015**, *15*, 4129–4134.
- (S5) Gloter, A. *et al. Eur. Phys. J. B* **2001**, *22*, 179–186.
- (S6) Kalavathi, S.; Serin, V.; Turquat, Ch.; Cesari, C.; Leroux, Ch.; Nihoul, G. *J. Phys.: Condens. Matter* **2014**, *26*, 015601.
- (S7) Wang, Y.; Khachaturyan, A. *Acta Mater.* **1997**, *45*, 759–773.
- (S8) Gu, Y.; Cao, J.; Wu, J.; Chen, L.-Q. *J. Appl. Phys.* **2010**, *108*, 083517.
- (S9) Quackenbush, N. F.; Paik, H.; Wahila, M. J.; Sallis, S.; Holtz, M. E.; Huang, X.; Ganose, A.; Morgan, B. J.; Scanlon, D. O.; Gu, Y.; Xue, F.; Chen, L.-Q.; Sterbinsky, G. E.; Schlueter, C.; Lee, T.-L.; Woicik, J. C.; Guo, J.-H.; Brock, J. D.; Muller, D. A.; Arena, D. A.; Schlom, D. G.; Piper, L. F. *J. Phys. Rev. B* **2016**, *94*, 085105.
- (S10) Li, Y.; Hu, S.; Liu, Z.; Chen, L. *Acta Mater.* **2002**, *50*, 395–411.
- (S11) Chen, L.; Shen, J. *Comput. Phys. Commun.* **1998**, *108*, 147–158.
- (S12) Noguera, C. *Physics and chemistry at oxide surfaces*; Cambridge University Press, 1996.
- (S13) Stoneham, A. *Appl. Surf. Sci.* **1983**, *14*, 249–259.
- (S14) Hlinka, J.; Marton, P. *Phys. Rev. B* **2006**, *74*, 104104.
- (S15) Meyer, B.; Vanderbilt, D. *Phys. Rev. B* **2002**, *65*, 104111.
- (S16) Meitl, M. A.; Zhu, Z.-T.; Kumar, V.; Lee, K. J.; Feng, X.; Huang, Y. Y.; Adesida, I.; Nuzzo, R. G.; Rogers, J. A. *Nature Mater.* **2006**, *5*, 33–38.
- (S17) Zhang, K.; Seo, J.-H.; Zhou, W.; Ma, Z. *J. Phys. D: Appl. Phys.* **2012**, *45*, 143001.